Vapor-to-Droplet Transition in a Lennard-Jones Fluid: Simulation Study of Nucleation Barriers Using the Ghost Field Method

Alexander V. Neimark* and Aleksey Vishnyakov

Center for Modeling and Characterization of Nanoporous Materials, TRI/Princeton, 601 Prospect Avenue, Princeton, New Jersey 08542

Received: August 10, 2004

We report a comprehensive Monte Carlo (MC) simulation study of the vapor-to-droplet transition in Lennard-Jones fluid confined to a spherical container with repulsive walls, which is a case study system to investigate homogeneous nucleation. The focus is made on the application of a modified version of the ghost field method (Vishnyakov, A.; Neimark, A. V. *J. Chem. Phys.* **2003**, *119*, 9755) to calculate the nucleation barrier. This method allows one to build up a continuous trajectory of equilibrium states stabilized by the ghost field potential, which connects a reference droplet with a reference vapor state. Two computation schemes are employed for free energy calculations, direct thermodynamic integration along the constructed trajectory and umbrella sampling. The nucleation barriers and the size dependence of the surface tension are reported for droplets containing from 260 to 2000 molecules. The MC simulation study is complemented by a review of the simulation methods applied to computing the nucleation barriers and a detailed analysis of the vapor-to-droplet transition by means of the classical nucleation theory.

1. Introduction

Liquid clusters and droplets in supersaturated Lennard-Jones (LJ) vapor were among the first inhomogeneous systems studied using Monte Carlo (MC) and molecular dynamics (MD) simulation methods in the 1970s. Since then, several simulation techniques were invented for and applied to the calculation of the free energy of critical droplets (nuclei), which determine the rate of nucleation.[1−11] However, despite multiple efforts, the problem of reliable simulations of droplet nucleation still remains in the focus of energetic discussions, which recently revealed essential controversies and shortcomings of earlier suggested simulation methods. The problem lies in the inherent instability of a nucleus in an open system, which makes it difficult to relate its free energy to the free energy of a thermodynamically stable reference state. Three basic approaches to computing the free energy of droplets have been presented in the literature: (i) *direct thermodynamic integration* by stabilizing the droplet in the canonical ensemble (closed system) and building a path of equilibrium configurations to a state with the free energy known exactly or estimated from a simple model (commonly an ideal vapor or an ideal crystal); (ii) *pressure tensor calculation* by stabilizing the droplet in the canonical ensemble and computing the surface energy from the radial profiles of normal and tangential pressures; (iii) *umbrella sampling in an open system* by generating droplets in a homogeneous system under the constant pressure or constant chemical potential conditions using a configuration bias. To emphasize the objective of our work, we start from a brief critical analysis of these methods.

1.1. Direct Thermodynamic Integration. One of the first simulation studies of the free energy of small clusters was done by McGinty in 1973,[12] who performed MD simulations of freezing and melting of small LJ clusters containing up to 100 atoms. The free energy of formation of solid clusters was found to be in agreement with the microcrystal model. Melting and freezing transitions in small droplets were modeled by Kristensen et al.[13] and then by Briant and Burton,[14] who concluded that the surface tension increases with the cluster size in accord with the Tolman equation.[15]

In their seminal paper,[2] Lee, Barker, and Abraham (LBA) performed canonical ensemble MC simulations of small LJ droplets (up to 100 molecules) in a metastable vapor confined to a finite volume cell. To find the Helmholtz free energy of the droplet, a series of simulations were performed in which the size of the confining cell was gradually increased, keeping the number of molecules fixed, until the vapor state was reached. The Helmholtz free energy was found from the volume dependence of the pressure, assuming that the $p\ \mathrm{d}V$ integral along this pass gives the reversible work of droplet formation. The pressure was determined by the virial equation. Later, Lee et al.[16] applied the Barker−Henderson perturbation theory[17−19] to the free energy of liquid LJ clusters and found the results in agreement with the molecular simulations. Another route to generate a trajectory of equilibrium states for thermodynamic integration was undertaken by Garcia and Torroja,[20] who gradually heated the cluster until it evaporated. Then, the free energy was obtained by integration from a vapor state at a high temperature.

The LBA approach[2] was used in several later publications.[21−23] Oh and Zeng[22] studied the influence of the mobility of the cluster center of mass on the free energy predicted earlier by Reiss et al.[24] Reguera et al.[23] considered the vapor-to-droplet transition in a small spherical NVT system and calculated the Helmholtz free energy from the dependence of the pressure on the cell volume at a constant loading. The authors[23] discussed the importance of accounting for the cluster motion. Because the size of the simulation cell is comparable with the size of the cluster, the configurations, in which the cluster approaches the cell wall, have a nonzero statistical weight. The authors

* Author to whom correspondence should be addressed. E-mail: aneimark@triprinceton.org

10.1021/jp0464066 CCC: $30.25
Published on Web 03/05/2005

introduced a "extended modified liquid drop" model, which was found to be in good agreement with the MC data.

The LBA approach is based on the assumption that a droplet in a finite system can be formed reversibly in the process of decreasing the system volume at a constant loading. However, as was shown first by Binder and co-workers[25,26a] for the Ising model, demonstrated by Kieeling and Percus[26b] with nonuniform van der Waals theory, and discussed recently in detail by Requera et al.[23] for the LJ fluid, the vapor-to-droplet transition in a finite system contains a spontaneous step. Thus, it is not possible to construct a truly continuous trajectory of equilibrium states in the canonical ensemble, which would connect a droplet state with a reference vapor state. Earlier works necessarily employed an interpolated trajectory unless the simulation temperature was sufficiently close to the critical temperature. Moreover, Reiss and Reguera[27] recently questioned the validity of the virial equation for a heterogeneous system confined to a small volume. Without application of the virial equation, the pressure can be apparently estimated from the vapor density on the periphery of the cell, as done, for example, in ref 3; however this intuitive method cannot be justified for small simulation cells either. The Widom insertion method[28] seems to be the best scientifically sound approach to computing the chemical potential in canonical ensemble simulation; however its practical accuracy is not sufficient for dense and inhomogeneous systems such as liquid clusters.[29]

1.2. Pressure Tensor Calculation. Direct calculation of the pressure tensor is probably the most popular method for computing the surface free energy of liquid clusters, which was introduced by Rusanov and Brodskaya (RB)[3] in 1977. The authors computed the normal component of the Irving−Kirkwood[30] pressure tensor of small LJ droplets of various sizes (up to 500 molecules) in a series of MD simulations. The work of cluster formation and, respectfully, the surface tension of the spherical interface was calculated by integrating the pressure tensor. This technique was employed later by Thomson et al.,[31] who performed comprehensive MC and MD simulations of larger (up to 2048 molecules) droplets and obtained the surface tension and the location of the surface of tension. The results were qualitatively very similar to those of ref 3. The surface tension was an increasing function of the droplet radius of tension that implied a positive Tolman length. Nijmeijer et al.[4] simulated even larger (up to 12 000 molecules) clusters. The authors derived an expression for the surface tension, the radius of tension, and the Tolman length from the normal and tangential components of the pressure tensor. In contrast to the results of refs 3 and 31, they obtained small negative values of the Tolman length with large deviations due to statistical errors in the tangential component. In subsequent discussion,[32,33] Brodskaya and Rusanov revisited the data of Nijmeijer[33] and came to positive values of the Tolman length. Later, Haye and Bruin[34] obtained a positive value of the Tolman length for a similar cluster at higher temperature. Recently, el Bardouni et al.[35] calculated pressure profiles across flat, cylindrical, and spherical interfaces and concluded that the surface tension is independent of the interface shape.[35]

An apparent inconsistency of the results reported in the literature shows that the pressure tensor method is questionable in nanoscale systems. It is worth noting that most authors, including Brodskaya and Rusanov,[3] assumed an ideal interpretation of reference liquid and vapor phases (ideal vapor and incompressible liquid) that in our experience should have affected the calculated free energies substantially. Moreover, ten Wolde and Frenkel[5] questioned the very validity of the pressure tensor calculations for small droplets. They demonstrated a striking disagreement with the results of the constant-pressure MC simulation of LJ droplets. In our recent study,[36] we performed MD simulations to calculate the nucleation barrier in accord with the RB method[3] and found a qualitatively similar discrepancy with the results of MC simulations rendered in accord with the approach employed in this work, thus confirming that the mechanical approach based on the calculation of the pressure tensor is inconsistent with the thermodynamic interpretation of the results of MC simulations.

1.3. Umbrella Sampling in an Open System. Ten Wolde and Frenkel[5] suggested constant-pressure MC simulations with a configuration bias as a practical alternative to methods based on the canonical ensemble. Clusters, which emerge in an open system as fluctuations, were sampled by imposing a fictitious potential that depended on the cluster size. To calculate the cluster free energy, the authors employed the umbrella sampling technique.[29,37] The size dependence of the droplet free energy was derived from the droplet size distribution. Although the umbrella sampling technique has a rigorous statistico-mechanical foundation, it is computationally demanding. It is worth noting also that the biasing potential depends on an accepted definition of molecular clusters, which has a geometrical rather than a thermodynamic nature. In this work, we employed the data of ref 5 to verify the MC approach that we developed.

Chen et al.[38] employed a combination of an aggregation-biased MC technique[10,39] and umbrella sampling to determine the nucleation barriers for LJ clusters composed of up to 300 molecules. The authors demonstrated the computational efficacy of their method. The results of ref 38 compare well with those of refs 5 and 22. Kusaka et al.[7] employed a grand canonical MC (GCMC)[40] simulation with restricted number of molecules and estimated the free energy from a probability of observation of the cluster of a given size. Later, Kusaka and Oxtoby[6] presented another approach that did not involve a cluster criterion but explored the stochastic evolution of the metastable vapor phase with emerging clusters in GCMC simulation aided by the umbrella sampling. The authors attained a coarse-grained description of the stochastic process by introducing proper order parameters (loading and potential energy) and evaluated the free energy of cluster formation as a function of the order parameters. The statistical weights of the molecular configurations were modified to favor the formation of large clusters, which would have a negligible chance to appear in unbiased simulations. From the distributions of cluster sizes, the authors derived the dependence of the free energy on the cluster size. Several methods employed calculations of free energy gains caused by adding a molecule to a cluster. For example, Hale[41] calculated the configurational Helmholtz free energy differences between clusters consisting of n and $n - 1$ molecules. From this "free energy profile", he obtained the entropy and effective surface tension.

Although the umbrella sampling techniques are the best currently available methods for calculating the cluster free energy, the biasing potential depends on an accepted cluster criterion, which has a geometrical rather than a thermodynamic nature. Different cluster criteria employed in different methods may affect the results of simulations and cause deviations of reported data.[38]

In this work, we demonstrate a new MC simulation approach to generate critical nuclei in a metastable vapor and to determine the nucleation barriers. We consider the vapor-to-liquid transition in LJ fluid confined to a spherical cell with repulsive walls. The approach, which technically could be associated with direct

thermodynamic integration, is free of the shortcomings of the techniques discussed above. It exploits two simulation methods that we introduced recently and applied to modeling phase transitions in small pores: the *gauge cell method*,[42,43] in which clusters are stabilized by restricting the range of allowed density fluctuations and the chemical potential of the cluster is measured directly, and the *ghost field method*,[11] in which a potential well of tunable magnitude is introduced to construct a continuous trajectory of states connecting a reference cluster and a low-density vapor state and the cluster free energy is computed by the thermodynamic integration along this trajectory. The focus is on the implementation and technical details of the ghost field method.

The rest of the paper is structured as follows. In section 2 we employ the capillarity approximation of the classical nucleation theory (CNT) and qualitatively analyze the specifics of the vapor-to-liquid transition in a finite volume, emphasizing the key problems to be addressed in molecular simulations. Section 3 describes the model systems considered in MC simulations and the simulation details of the gauge cell method and the ghost field methods employed. Simulation results and free energy calculations are presented in section 4. The nucleation barriers and the surface tension of droplets of LJ fluid are discussed in section 5. Conclusions are given in section 6.

2. Vapor-to-Droplet Transition in a Finite Volume: An Insight from the Classical Nucleation Theory

2.1. D-Droplets, E-Droplets, and Superspinodal. In this work, we study the vapor-to-droplet transition in a LJ fluid confined to a spherical cell of radius R and volume $V = {}^4/_3\pi R^3$. To highlight the main problem to be addressed in simulations, let us start from the capillarity approximation of the classical nucleation theory,[44−46] which represents a liquid cluster as a spherical droplet (CNT model). In the thermodynamic approach of Gibbs, the density and the pressure in the droplet as well as the density and the pressure in the surrounding vapor are assumed to be uniform up to the dividing surface. The condition of chemical equilibrium implies that the pressures p_l and p_v and densities ρ_l and ρ_v of these uniform phases correspond via the equation of state to the respective phases at a given chemical potential μ. The droplet radius r is defined from the mass balance, namely,

$$N_d(\mu) = \rho_v(\mu)V + \frac{4}{3}\pi r^3[\rho_l(\mu) - \rho_v(\mu)] \qquad (1)$$

where $N_d(\mu)$ is the total number of molecules in the cell distributed between the droplet and the vapor. The second summand in the right-hand side of eq 1 represents the excess droplet mass, $\Delta N^*(\mu)$, which does not depend on the cell volume. The condition of the mechanical equilibrium is given by the Laplace equation,

$$\Delta p = \frac{2\gamma}{r} \qquad (2)$$

where $\Delta p = p_l - p_v$ is the pressure difference between the liquid inside the droplet and vapor outside and γ is the surface tension.

In the CNT model used below, the difference between the equimolar radius defined by eq 1 and the radius of tension, which should be employed in eq 2, is ignored as well as the radius dependence of the surface tension. For the latter, we assume the planar value of the surface tension, γ_∞, determined in MC simulations. Within these assumptions, eqs 1 and 2 give the isotherms of LJ droplets confined to a finite volume. A series of the droplet isotherms in the cells of different radii are presented in Figure 1 as the average fluid density in the cell $\rho = N/V$ reduced to the molecular diameter cubed, $\rho\sigma^3$, versus the supersaturation p_v/p_0. To provide the closest fit to the MC simulation results and to avoid additional errors related to the conventional assumptions of an ideal vapor and of an incompressible liquid, we employ the equation of state of a LJ fluid by the equation of Johnson, Zolveg, and Gibbins (JZG),[47] which takes into account the particular model employed for the intermolecular potential. We assume a LJ fluid with 5σ cutoff at $kT/\epsilon = 0.7625$, which is studied below in MC simulations. The surface tension γ_∞ is the most sensitive parameter. Different values of γ_∞ were reported in the literature for these conditions. Figure S1 (Supporting Information) shows the dependence of γ_∞ on the temperature and the cutoff distance. We interpolated the results of different authors,[38,48,49] assuming that γ_∞ is a linear function of ϵ/kT, and obtained values from 0.888 to 0.92 ϵ/σ^2. The value of $\gamma_\infty = 0.91\ \epsilon/\sigma^2$ [48] was used in calculations.

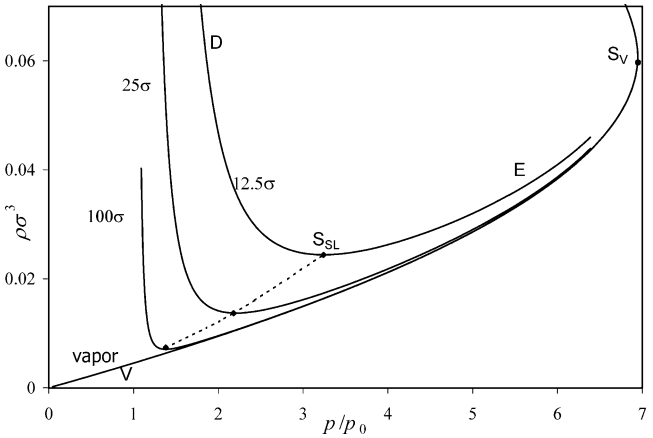

Figure 1. Isotherms of droplets and vapor configurations in spherical cells of different radii (shown in the chart) with hard walls calculated using the CNT. Superspinodals S_{SL} the states of zero compressibilty, correspond to the minima of droplet isotherms, which separate D-droplets and unstable E-droplets. The CNT does not work in the vicinity of the vapor spinodal S_V.

As the supersaturation increases, the droplet size decreases in accord with eq 2 whereas the vapor is getting denser. As a result of the competition of these effects, the droplet isotherms are nonmonotonic, Figure 1. At lower pressures, the density change with the increase of the vapor pressure is determined by droplet contraction, while at higher pressures the contribution from the droplet becomes negligible and the isotherm approaches the isotherm of bulk vapor (solid line). The bulk vapor isotherm, which was also calculated by the JZG equation, terminates at the vapor spinodal S_V reached at pressure $p_v = p_{S_V} = 0.0231\ \epsilon\sigma^{-3}$ ($p_v/p_0 = 6.95$), where the vapor compressibility diverges. It should be noted that the CNT model with a constant surface tension does not work at the vapor spinodal, and we do not attempt to explore near-spinodal regions using this model.

The droplet isotherm $\rho(p_v)$ has a minimum at point S_{SL} where the vapor densification offsets the droplet shrinking. The system compressibility $(\partial\rho/\partial p_v)_{V,T}$ increases monotonically from negative values for large droplets (low pressures) to positive values for smaller droplets (high pressures). The minimum S_{SL} corresponds to a state of zero compressibility $(\partial\rho/\partial p_v)_{V,T} = 0$. Note that here we are discussing the compressibility of the whole system, droplet and vapor, rather than compressibility of a solitary droplet, which is always negative. By analogy with the

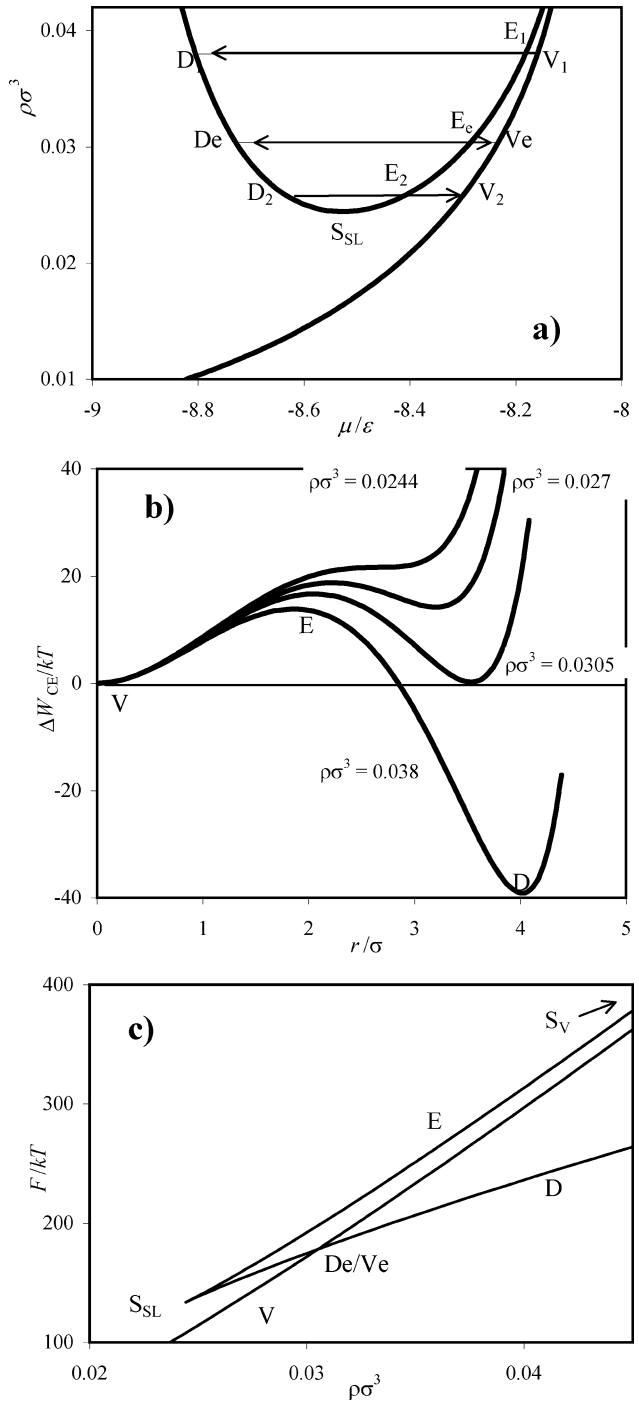

Figure 2. (a) Vapor and droplet isotherms in a $R = 12.5\sigma$ pore calculated using CNT. D, stable/metastable droplet configurations; V, vapor configurations; E, unstable droplet configurations. V_e-D_e states correspond to the vapor−droplet equilibrium. Superspinodal S_{SL} separates D and E droplets. (b) The work of droplet formation as a function of droptet radius r at constant loading $\Delta W_{VD} > 0$ at $\rho\sigma^3 = 0.038$, $\Delta W_{VD} < 0$ at $\rho\sigma^3 = 0.027$ and VDE corresponds to $\rho\sigma^3 = 0.0305$ at $\Delta W_{VD} = 0$. The minima correspond to vapor ($r = 0$) and D droplets; the maxima correspond to E-droplets that play the role of critical embryos and determine the height of nucleation barrier for vapor−droplet transition (c) Helmoholtz free energy vs loading for vapor, D-droplet, and E-droplets states. The intersection of the V and D branches correspond to the vapor−droplet equilibrium.

spinodal as a state of diverging compressibility, we refer to a state of the vanishing compressibility as *superspinodal*.[50a] The superspinodal determines the lowest density of the system at which a droplet state can exist. Thus, in the range of densities between the vapor spinodal and the superspinodal, $\rho_{S_V} > \rho > \rho_{S_{SL}}$, the CNT model gives three different states at the same density: "large" droplet D in a "low" density vapor (Figure 2), "small" droplet E in a denser vapor at a higher pressure, and vapor V at an even higher pressure.

As was shown by Binder and Kalos,[25,26a] who studied vapor-to droplet transition in the Ising lattice model, and thoroughly discussed recently by Reguera et,[23] who studied a LJ fluid, the E-droplets are entirely unstable even in the closed system. This means that an E-droplet is unstable with respect to infinitesimally small local fluctuations of the fluid density. In fact, an E-droplet plays the role of a critical embryo (this is why we named it an E-droplet) in the vapor-to-droplet transition resulting in a D-droplet, which occurs at a constant loading.

2.2. Free Energy Analysis and Nucleation Barriers. Let us consider the work of formation ΔW_{CE} of the spherical droplet of radius r in a vapor confined to a finite volume.[50b] The subscript "CE" indicates that the system is considered in the canonical ensemble at fixed N, V, and T. $\Delta W_{CE}(r)$ represents the difference of the Helmholtz free energy of the vapor with the droplet of radius r,

$$F_d = -\left(V - \frac{4}{3}\pi r^3\right)p_v(\mu) - \frac{4}{3}\pi r^3 p_l(\mu) + \mu N + 4\pi r^2\gamma \quad (3)$$

and that of the initial vapor state V without a droplet,

$$F_v = -V(p_v(\mu_V) + \mu\rho_v(\mu_V)) \quad (4)$$

$$\Delta W_{CE}(r) = F_d(\mu) - F_v(\mu_V) \quad (5)$$

In eq 3, the condition of chemical equilibrium between the liquid in the droplet and the vapor is assumed explicitly so that the liquid and vapor pressures $p_{l/v}$ and densities $\rho_{l/v}$ are parametrized by the same chemical potential μ in accord with the equation of state for bulk phases. μ is related to the droplet radius r through the equation of mass balance,

$$N = \rho V = \rho_d(\mu)V = N_d(\mu) = \rho_v(\mu)V + \frac{4}{3}\pi r^3[\rho_l(\mu) - \rho_v(\mu)] = N_v(\mu_V) = \rho_v(\mu)V \quad (6)$$

Equation 6 implies that the droplet formation (dissolution) in the process of vapor-to-droplet (droplet-to-vapor) transition occurs at constant loading N or at a constant overall density $\rho = N/V$, as $V =$ constant. Vapor-to-droplet and droplet-to-vapor transitions correspond to horizontal lines in Figure 2a, where the isotherms in the $R = 12.5\sigma$ cell are presented in coordinates, loading N (total number of molecules) versus chemical potential μ.

The work of droplet formation $\Delta W_{CE}(r)$ as a function of the droplet radius is given in Figure 2b (to be specific we present calculations for the 12.5σ cell). At $\rho > \rho_{S_{SL}}$, it has a maximum and a minimum determined from the condition, $\partial F_d/\partial r|_{N,V,T} = 0$, which, as follows from the direct differentiation of eq 3 with taking into account the Gibbs−Duhem equations, $\partial p_{l/v}/\partial\mu|_T = -\rho_{l/v}$, implies the Laplace eq 2 reflecting mechanical equilibrium between the droplet and the vapor, $\Delta p = p_l - p_v = 2\gamma/r$. Thus, the maxima and minima of $\Delta W_{CE}(r)$ correspond to equilibrium droplet states, E and D, defined by eqs 1 and 2. By substitution of the Laplace eq 2 into eq 3, the Helmholtz free energy of an equilibrium droplet state reduces to

$$F_d = -Vp_v(\mu) + \mu N + \frac{4}{3}\pi r^2\gamma \quad (7)$$

The minimum of the work of droplet formation corresponds to the large droplet state D on the droplet isotherm depicted in Figure 2b. Depending on the loading N, the minimum of $\Delta W_{CE}(r_d)$ can be either negative, positive, or zero. Negative $\Delta W_{CE}(r_d)$ corresponds to the droplet states that have a smaller Helmholtz free energy than that of the vapor state at the same loading, $F_D < F_V$. Therefore, the vapor-to-droplet transition is energetically favorable and leads to a stable droplet, transition $V_1 \rightarrow D_1$ in Figure 2a. Positive $\Delta W_{CE}(r_d)$ corresponds to the droplet states that have a larger Helmholtz free energy than that of the vapor state at the same loading, $F_d > F_V$. In this case, the droplet-to-vapor-transition is energetically favorable and leads to a stable vapor state, transition $D_2 \rightarrow V_2$ in Figure 2. The condition $\Delta W_{CE}(r_d) = 0$ corresponds to the vapor−droplet equilibrium (VDE) in the closed system in a sense that $F_d = F_V$, transition $D_e \rightarrow V_e$ in Figure 2a. The maximum work of droplet formation corresponds to a small droplet E. Thus, an E-droplet is entirely unstable; any fluctuation of its size is energetically favorable. It is worth noting again that we are considering a closed system, in which conditions of stability are different from those in an open system; any droplet state would be unstable in an open system.

Stability analysis of droplet and vapor states in the closed system is illustrated by the plot of the variation of the Helmholtz free energy along the droplet and vapor isotherms as a function of the loading given in Figure 2c. The point of intersection of droplet and vapor branches corresponds to the VDE. At larger loadings, $N > N_e$, $F_D < F_V$. D-droplet states are stable, and vapor states are metastable. At smaller loadings, $N_{S_{SL}} > N < N_e$, $F_D > F_V$, D-droplet states are metastable, and vapor states are stable. The left turnover point, which corresponds to the superspinodal S_{SL}, separates metastable D-droplets and unstable E-droplets located on the upper branch $S_{SL}S_V$. The Helmholtz free energy of the E-droplet states exceeds those of D-droplet states and the vapor states at the same loading.

The work of formation of the unstable droplet E_1 represents the nucleation barrier for the formation of the stable droplet D_1 in the closed system of volume V. That is to say that the nucleation barrier of the vapor-to-droplet transition is determined by

$$\Delta W_{VD}(N,V,T) = \Delta W_{CE}(r_E) = V(p_v(\mu_V) - p_v(\mu_E)) - (\mu_V - \mu_E)N + \frac{4\pi}{3} r_E^2 \gamma \quad (8)$$

The difference between the Helmholtz free energies of the metastable stable droplet D_2 and the unstable droplet E_2 determines the nucleation barrier for the droplet-to-vapor transition,

$$\Delta W_{DV}(N,V,T) = F_d(\mu_E) - F_d(\mu_V) = V(p_v(\mu_V) - p_v(\mu_E)) + (\mu_E - \mu_V)N - \frac{4\pi}{3}(r_D^2 - r_E^2)\gamma \quad (9)$$

At the superspinodal S_{SL}, the nucleation barrier for the droplet-to-vapor transition vanishes, thus indicating the lower limit of metastable D-droplets in the closed system. At the VDE, the nucleation barrier for the droplet-to-vapor transition equals the nucleation barrier for the vapor-to-droplet transition. The VDE condition reads

$$V(p_v(\mu_{Ve}) - p_v(\mu_{D_e})) - (\mu_{V_e} - \mu_{De})N_e + \frac{4\pi}{3} r_{D_e}^2 \gamma = 0 \quad (10)$$

We should note that the nucleation barriers eqs 7 and 8 determine the rates of vapor-to-droplet and droplet-to-vapor transitions in the closed system of volume V. In an open system, for example, in a supersaturated vapor kept at constant chemical potential in the grand canonical ensemble, the nucleation barrier for the vapor−liquid transition is given by the Gibbs formula

$$\Delta\Omega_d = \frac{4\pi}{3} r^2 \gamma = \frac{2\pi}{3} \Delta p r^3 = \frac{16\pi\gamma^3}{3(\Delta p)^2} \quad (11)$$

$\Delta\Omega_d$ represents the difference of the grand thermodynamic potentials of a fixed volume V of the vapor with the droplet, $\Omega_d = -(V - {}^4/_3\pi r^3)p_v - {}^4/_3\pi r^3 p_l + 4\pi r^2\gamma$, and without, $\Omega_v = -Vp_v$.

2.3. Lessons from the CNT Analysis. Albeit being an approximate theory, the CNT model shows the main problems to be addressed in molecular simulations of droplet nucleation in a closed system. For a given cell volume V, there exists a lower limit of droplet sizes, $r_{S_{SL}}$, which can be stabilized and studied in the closed system. This limit corresponds to the superspinodal S_{SL}, the minimum point on the droplet isotherm, which separates metastable D-droplets of $r > r_{S_{SL}}$ and labile E-droplets of $r < r_{S_{SL}}$. To study smaller droplets, the cell size must be reduced. The dependence of $r_{S_{SL}}$ on the cell volume is given in Figure S2 (Supporting Information). Above the superspinodal, the vapor and droplet states at the same loading are separated by an energy barrier that corresponds to the work of formation of an E-droplet, eqs 7 and 8. Only when the nucleation barrier at the VDE, $\Delta W_{VDE}(N,V,T)$, is small enough (in our experience not exceeding several kT for simulation runs of several million MC steps), it is feasible to sample the whole configuration space and to construct a continuous isotherm connecting droplet and vapor states. Such small nucleation barriers are observed only in very small volumes or in the vicinity of the critical temperature. Thus, if $\Delta W_{VDE}(N,V,T)$ is low enough and the simulation is long enough, then a sequence of jumps between D-droplets and vapor over E-droplet states can be sampled in a single CEMC simulation, and the simulated continuous isotherm exhibits a rounded step. This situation is similar to that found in GCMC simulations of capillary condensation in narrow pores.[43] In this case, the free energy of droplets and, respectively, the nucleation barriers can be calculated by the thermodynamic integration as was done in refs 2, 22, and 23.

For practical applications, the most interesting range of nucleation barriers is $20-100kT$. These barriers cannot be overcome in unbiased MC simulations. That is to say that in CEMC simulations we should expect to observe a hysteresis. Due to a finite length of the simulation run, the sampling is confined either to the domain of vapor configurations or to the domain of D-droplet configurations. With the decrease of loading from a stable D-droplet state, a spontaneous evaporation occurs at some point between the VDE and the superspinodal S_{SL} and vice versa. With the increase of loading from a stable vapor state, a spontaneous condensation occurs at some point between the VDE and the vapor spinodal S_V. The resulting hysteresis loop may look similar to the loop $D_1V_1V_2D_2$ in Figure 2a.

A discontinuous droplet-to-vapor transition in a finite volume was first demonstrated by Binder and Kalos using a ferromagnetic Ising lattice.[25,26a] Reguera et al. found a discontinuity of droplet evaporation in a LJ fluid at a constant loading as the cell volume increased.[23] This process is similar to the process of droplet evaporation in a cell of a fixed volume as the loading decreases, which we consider here. To demonstrate this similarity, we show in Figure 3a the droplet and vapor isotherms at

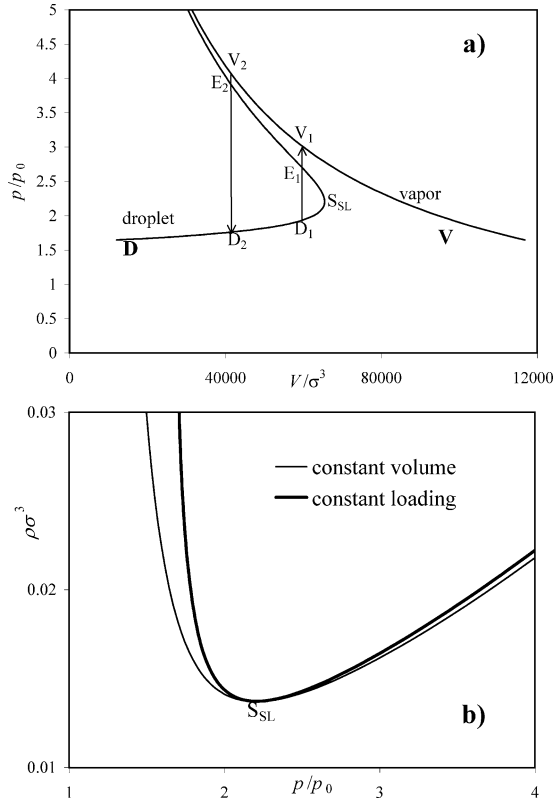

Figure 3. (a) Isotherms of droplet and vapor states at constant loading $N = 895$ and variable volume V calculated using the CNT. Arrows indicate vapor−droplet and droplet−vapor transitions (b) Droplet isotherms at constant loading ($N = 895$) and constant volume ($R = 25\sigma$) conditions. The isotherms coincide at the minimun showing that the superspinodal behavior does not depend on the route of varying the supersaturation.

constant loading $N = 895$, which corresponds to the S_{SL} at $R = 25\sigma$. This plot is quite similar to that of ref 23. The turnover point S_{SL} is a superspinodal point of vanishing compressibility, which separated metastable D-droplets and labile E-droplets. Figure 3a may be rebuilt in $\rho - p_v$ coordinates (Figure 3b). The isotherm at the fixed loading ($N = 895$) has the same superspinodal as the isotherm in the fixed volume ($R = 25\sigma$). That is to say that the droplets smaller than $r_{S_{SL}}$ corresponding to the superspinodal cannot be simulated at either $N =$ constant or $V =$ constant.

To conclude, the superspinodal behavior makes it impossible in CEMC simulation to build a continuous path of equilibrium configurations connecting droplet states and vapor states because it would necessarily include inherently unstable configurations of E-droplets, which correspond to maxima of the Helmholtz free energy. Integration along the excess isotherm of D-droplets gives the variation of the nucleation barrier with the droplet size according to the general thermodynamic equation that stems from the nucleation theorem,[51,52]

$$\Delta\Omega(\mu) = \Delta\Omega(\mu_R) - \int_{\mu_{DR}}^{\mu} \Delta N^*(\mu)\, d\mu \qquad (12)$$

Here, $\Delta\Omega(\mu_R,T)$ is the nucleation barrier for the reference droplet at a certain chemical potential $\mu_R$that serves as a reference droplet state R. Because the isotherm of the D-droplets terminates abruptly, the nucleation barrier of the reference droplet has to be estimated independently. To calculate the nucleation barrier of a selected droplet, we employ the ghost field method.[11] This method allows us to construct a continuous

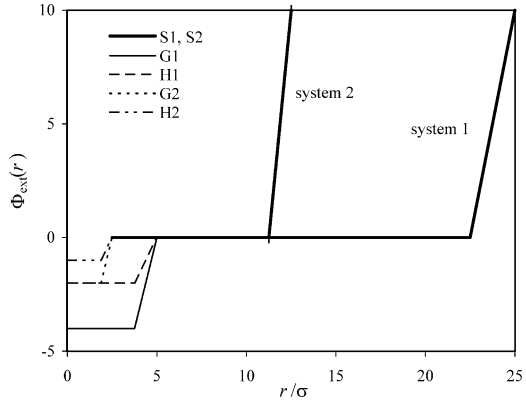

Figure 4. External potential field applied in Monte Carlo simulations for systems 1 and 2. Bold solid lines S1 and S2 show the soft repulsion from the walls. Thin lines show the ghost field profile in different systems. G1 (solid), -4ϵ potential well in system 1; H1 (dashed), -2ϵ potential well in system 1; G2 (dotted), -2ϵ potential well in system 2; H2 (dashed−dotted), -1ϵ potential well in system 2.

trajectory connecting a vapor state and the reference droplet state and to calculate its free energy by thermodynamic integration.

3. Simulation Details

3.1 Model Systems. We studied vapor-to-droplet transition in a Lennard-Jones (LJ) fluid confined to a spherical cell with repulsive walls (called below the pore) to prevent heterogeneous nucleation. To provide a potential opportunity for comparison of the simulation results with experimental data, most simulations and a detailed analysis of the host field method employed for calculating the nucleation barrier were performed for a LJ model nitrogen[53] at its normal boiling temperature of 77.4K (system 1). To compare our approach with previously published data, we also simulated the system studied by ten Wolde and Frenkel[5] (system 2). The parameters of these two systems are as follows.

System 1 (Model Nitrogen). Relatively large droplets ($N = 800-1900$ molecules) in a 25σ pore cell and a LJ fluid with the cutoff at 5σ at $kT/\epsilon = 0.7625$ were used. The wall exerted a repulsive potential as shown in Figure 4: $\Phi_{sf}(r) = 0$ at $r < 22.5\sigma$ and $\Phi_{sf}(r) = 4\epsilon(r - 22.5\sigma)$ at $r > 22.5\sigma$.

System 2 (ten Wolde and Frenkel Fluid). Smaller droplets ($N = 270-600$) in a 12.5σ pore cell and a LJ fluid with the cutoff at 2.5σ at $kT/\epsilon = 0.741$ were used. Ten Wolde and Frenkel reported for this system the saturation pressure $p_0 = 7.83 \times 10^{-3}\ \epsilon/\sigma^3$ that is ca. 2% lower than the value of $p_0 = 8.01 \times 10^{-3}\ \epsilon/\sigma^3$ given by the JZG equation of state.[47] The wall exerted a repulsive potential as shown in Figure 4: $\Phi_{sf}(r) = 0$ at $r < 2.5\sigma$ and $\Phi_{sf}(r) = 2\epsilon(r - 11.5\sigma)$ at $r > 11.5\sigma$.

The vapor states, which are metastable in an open system, were simulated by the standard grand canonical MC (GCMC) method. The droplets, which are unstable in an open system, were simulated using the gauge cell MC method.[42,43]

3.2. Gauge Cell MC Method. In the gauge cell MC method,[42,43] the simulation is performed simultaneously in two cells, which are in chemical equilibrium at isothermal conditions. One of the cells represents the pore, and the other is a gauge cell of a limited capacity. Mass exchange between the cells is allowed; however, the cell volumes are kept unchanged. The density fluctuations in the pore are controlled by the gauge cell capacity (volume). In the limit of infinite capacity, the gauge cell method is equivalent to the grand canonical MC (GCMC) method. In the limit of vanishing capacity, it is equivalent to

the canonical ensemble MC (CEMC) method. Choosing the ratio of the gauge cell and pore volumes sufficiently small, one can stabilize the fluid in a droplet state, which would be unstable in an open system. The chemical potential of the droplet state is assigned equal to the chemical potential measured in the gauge cell in accord with the JZG equation. Thus, the gauge cell has two functions, to prevent undesirable growth or decay of droplets and to measure their chemical potential. Note that with the gauge cell method one constructs the canonical ensemble isotherm $N(\mu)$ in the closed system.

A cube with triply periodic boundary conditions was employed as the gauge cell. The linear size of the gauge cell was at least 40σ and was adjusted so that a sufficient number of fluid molecules was contained in the gauge cell during the simulation. The number of molecules in the gauge cell varied from 40 to 100. The standard simulation length was about 5×10^4 MC steps per molecule for system 1 and about 2×10^5 per molecule for system 2. Each step included one attempt of molecule displacement in each cell and two attempts of molecule transfer between the cells. A constant external field was applied in the gauge cell to avoid fluid condensation in the gauge.

The internal structure of the droplet was characterized by profiles of local density from the droplet center of mass. We did not constrict the droplet motion in the cell. Thus, the simulated droplet is an "RKC cluster" (after ref 24) rather than an "LBA" (after ref 2).[22]

3.3. Ghost Field MC Method. To calculate the nucleation barrier by integration of the excess droplet isotherm in accord with the nucleation theorem, eq 12, it is necessary to determine the nucleation barrier $\Delta\Omega(\mu_R,T)$ for a reference droplet state R. To this end, it is necessary to build up a continuous trajectory of equilibrium states, which would connect the reference droplet state to a state with known Helmholtz free energy. Since the droplet isotherm cannot be continued in the region of small droplet size due to their inherent instability, it is impossible to connect the droplet isotherm with a vapor state. Technically, it is possible to connect the droplet isotherm to a liquid state, a state at which the pore is completely filled by liquid. When this construction is possible, the free energy of the liquid state can be determined, e.g., by the Peterson−Gubbins technique[54] employed in studies of hysteretic capillary condensation in mesopores. However, this construction is feasible only for a very small system where the droplet size can be increased up to the size of the cell. Therewith, the droplet isotherm smoothly passes through a turnover point of the liquid spinodal and transforms into the liquid isotherm, as shown in our simulation of the 7.5σ cell (Supporting Information, Figure S3). However, the total number of molecules in the 25σ liquid droplet would be about 5×10^4, which is too large for simulation to be feasible.

We employ the ghost field method[11] to construct a continuous trajectory connecting the reference droplet state and a vapor state and to calculate its free energy by thermodynamic integration. The ghost field method was established to calculate the nucleation barriers for capillary condensation in cylindrical capillaries with wetting walls.[11] In this work, we focus of the technical details of the ghost method as applied to studies of droplet nucleation. The reference droplet is constructed in the following fashion. An external "ghost" field is introduced in the cell center to provide the continuous formation of the droplet state of a desired density. The ghost field represents a potential well $\zeta\Phi_G(\mathbf{r})$ of tunable magnitude ζ ($0 \le \zeta \le 1$). $\zeta = 1$ corresponds to the full scale ghost field; $\zeta = 0$ corresponds to its absence. That is to say that the fluid in the cell is subject to the external potential, which is a sum of the repulsive potential exerted by the pore walls, $\Phi_W(\mathbf{r})$, and the attractive potential well in the pore center with tunable depth, the ghost field $\zeta\Phi_G(\mathbf{r})$: $\Phi_{ext}(\mathbf{r}) = \Phi_W(\mathbf{r}) + \zeta\Phi_G(\mathbf{r})$. The profiles of the external potential with the full scale ghost field ($\zeta = 1$) are shown in Figure 4. The continuity of the potential in the radial direction was secured by a transition zone, where the field changes linearly. To check the method consistency, we probed two different ghost fields for each system. They differed in the depth of the potential well $\Phi_G(0)$: -4ϵ and -2ϵ in system 1 and -2ϵ and -1ϵ in system 2.

Starting from a low-pressure vapor state, we first perform a series of gauge cell (or GCMC when applicable) simulations to trace vapor condensation in the potential well ($\zeta = 1$), which occurs as the vapor pressure increases. Second, once the droplet state of the desired density N_R is achieved, the ghost field is turned off gradually, step-by-step in a series of CEMC simulations performed with incremental changes of the ghost field magnitude from $\zeta = 1$ to $\zeta = 0$, keeping N_R unchanged. That is to say that the reference D-droplet is continuously connected with the initial vapor state.

4. Simulation Results

4.1. Isotherms. The isotherms of the droplet and vapor states generated by the gauge cell MC simulation are shown in Figures 5a and 5b. The vapor branches of the isotherms practically coincide with those obtained from the JZG equation with the density corrected to the repulsion from the wall. The droplet isotherm is in semiquantitative agreement with the isotherm of the D-droplets predicted by the CNT model, eqs 1 and 2. In system 1, we started from a large cluster of about 1600 molecules ($r = 7.7\sigma$, about 1900 molecules in the cell) and traced the D-branch down to a small cluster of about 370 molecules ($r = 4.8\sigma$, about 800 molecules in the cell). As the loading decreases further, the droplet evaporates, and a transition to a vapor configuration occurs. Vice versa, when we gradually increase the density in the vapor phase, it experiences a spontaneous transition to a D-droplet at a higher density. A similar hysteretic behavior was observed in system 2. The spontaneous transitions between droplet and vapor states are shown by dotted arrows in Figures 5a and 5b.

In Figure 5c, we present the excess droplet isotherm $\Delta N^* = V(\rho_D(\mu) - \rho_V(\mu))$ derived from the droplet and vapor isotherms in system 2 and compare it with the data of ref 5 obtained using the umbrella sampling in NPT ensemble. At lower pressures (and larger clusters), the two simulation methods agree very well. However, our simulation gives a larger ΔN^* (which means a larger cluster) at the same supersaturation. The difference is more pronounced for small clusters. This discrepancy can be explained by the different definitions of the clusters employed. The authors[5] defined clusters using a geometrical criterion calculating the distances between the molecular centers. We rely on the purely thermodynamic definition of the excess mass, which is de facto an average over fluctuating cluster configurations sampled at the same loading in the gauge cell method. The smaller the cluster, the more important it is the role of cluster size fluctuations.

The density profiles $\rho(r)$ of the droplets calculated from the center of mass in system 1 are shown in Figure 6. They are typical for spherical clusters. Except for the smallest one, the droplets are large enough to have a constant density in the core region, where the average fluid density is approximately the same as that in the bulk liquid. Typical snapshots of droplet states are presented in Figure 7. The largest and the smallest droplets stabilized in the gauge cell method are given in Figures

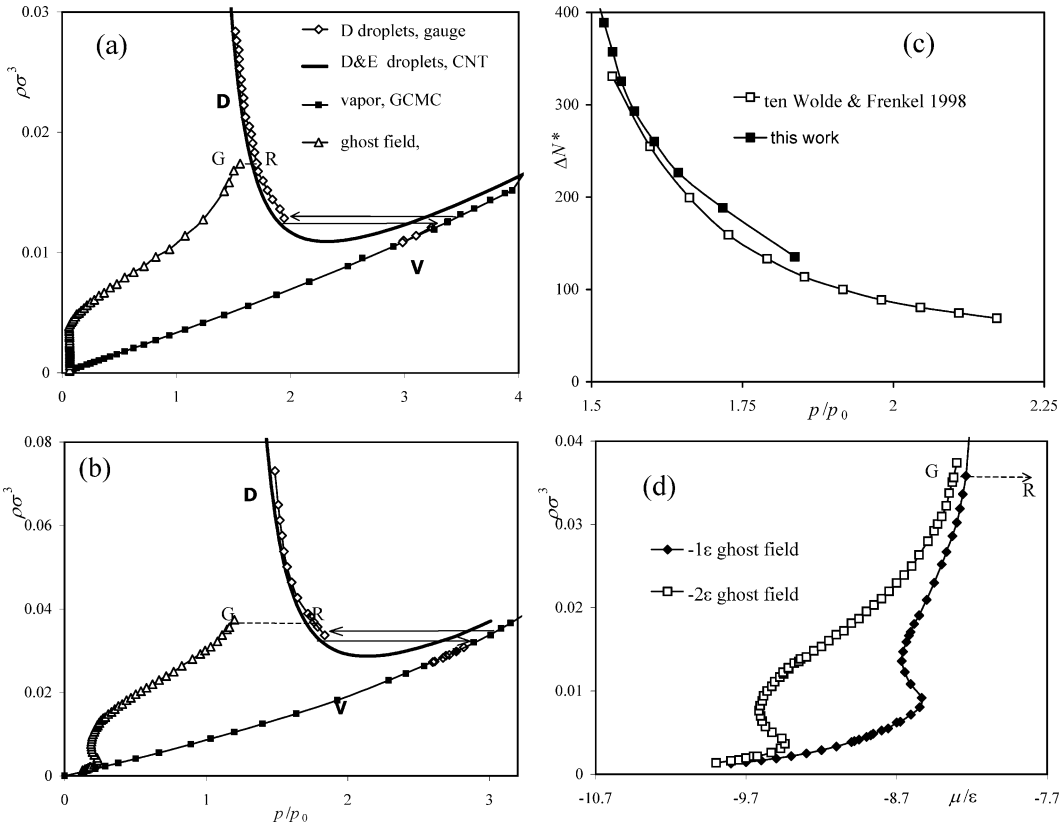

Figure 5. Simulated isotherms of the LJ droplets and vapor in (a) system 1 and (b) system 2. Point G is the droplet state stabilized in the full-strength ghost field ($\zeta = 1$); point R is the reference droplet state ($\zeta = 0$). The GR trajectory (horizontal dashed line) corresponds to ghost field removal at constant loading. Horizontal arrows indicate the transitions between vapor (V) and droplet (D) states. (c) Comparison between the excess isotherms of droplet states simulated in system 2 in this work and ref. (d) Isotherms of droplets stabilized in the ghost field (system 2). Van der Waals type loops correspond to condensation in the potential well.

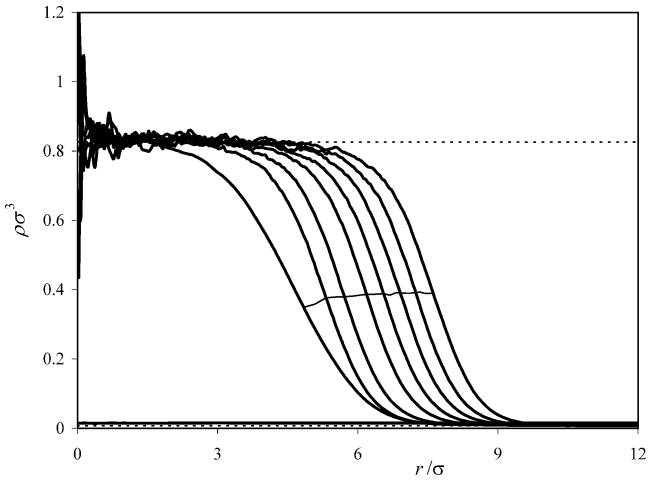

Figure 6. Density profiles of the LJ droplets of different sizes at $kT/\epsilon = 0.762$. The dotted line shows the densities of the bulk equilibrium liquid and vapor at saturation $p = p_0$. Thin solid lines show the locations of the equimolar dividing surfaces.

7a and 7b, respectively. In the vicinity of droplet−vapor transition, the cluster surface becomes rough, and the boundary between the cluster and the surrounding vapor becomes more diffuse (Figure 7b). The fluid density in the vapor region gradually decreases to a constant value, which is within ca. 5% of the bulk density at the same supersaturation. That is to say that the Gibbs construction is appropriate to determine in accord with eq 1 the equimolar droplet radius, which is marked by a dotted line.

The adsorption isotherms $\rho(\mu)$ in the cell with the ghost field ($\zeta = 1$) obtained using the gauge cell method are shown in Figures 5a, 5b, and 5d. They all have a sigmoid shape characteristic to capillary condensation in small pores clearly seen in Figure 5d, where the isotherms are presented as functions of the chemical potential. We start the isotherm from an ideal gas state at a sufficiently low vapor density. A van der Waals loop corresponds to the vapor condensation in the ghost field potential well. For example, in system 1 with a -4ϵ well (open triangles in Figure 5a), at $\rho\sigma^3 = 3.4 \times 10^{-4}$ (22 molecules in the system) the fluid is vaporlike, but at $\rho\sigma^3 = 6.0 \times 10^{-4}$ (39 molecules) a small droplet already forms in the potential well (Figure 5a). As the vapor pressure increases, the droplet grows gradually, and at $\rho\sigma^3 = 1.74 \times 10^{-2}$ it achieves the size of the D-droplets that were observed without the ghost field. The isotherms in system 2 are qualitatively similar to those in system 1 (Figure 5).

In Figure 5d, we present two isotherms in system 2 that were obtained by applying ghost field potentials of different depths. As expected, in the deeper well, the condensation occurs at a lower pressure.

The droplet growth in the ghost field ($\zeta = 1$, curve G in Figures 5a and 5b) was stopped at point G (Figure 5a) once the loading N_R of the targeted reference droplet state R was achieved. The droplet formed in the ghost field has a higher density in the center due to the potential well and more distinct boundaries. Typical snapshots of the droplet grown in the ghost field ($\zeta = 1$, state G) and of the reference droplet ($\zeta = 0$, state R) are presented in Figures 7c and 7d, respectively. Density profiles are given in Figure 8. The sharp interface makes fluid

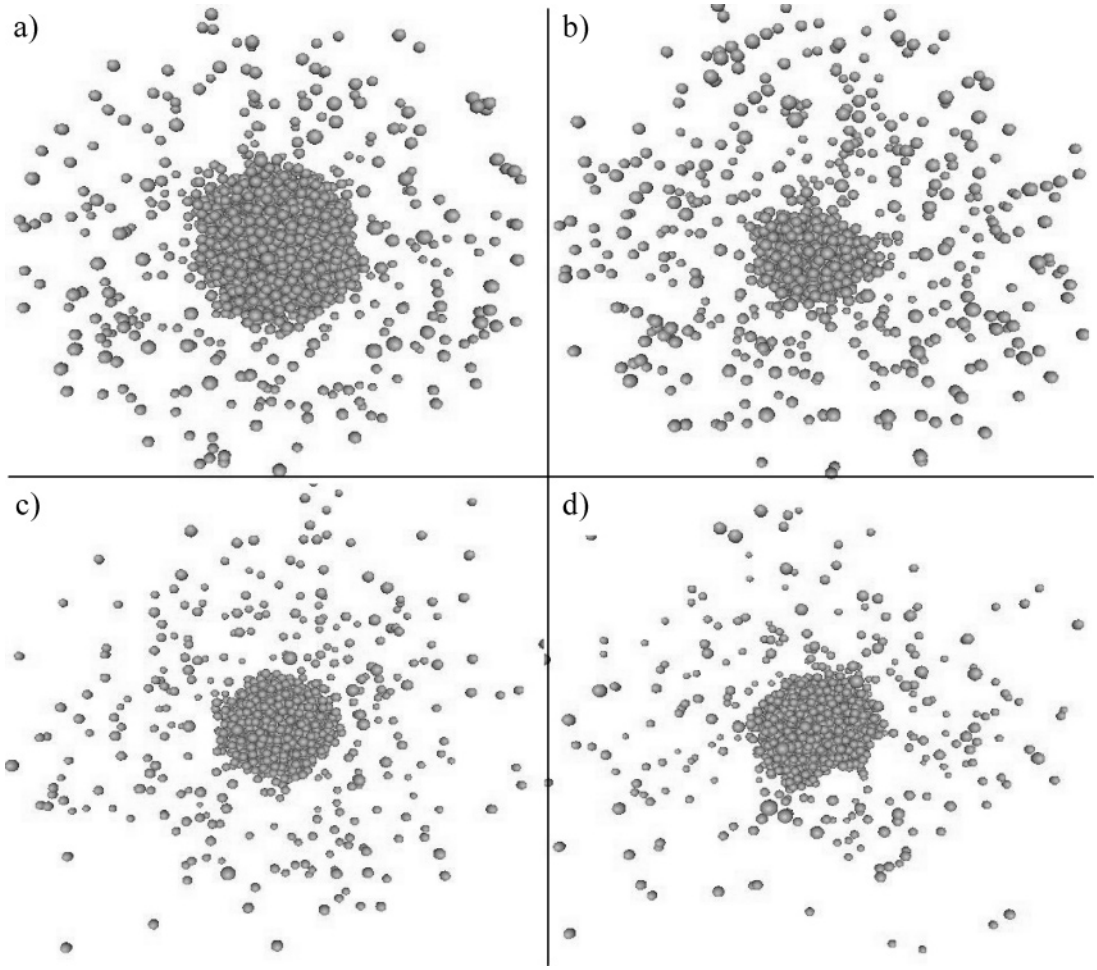

Figure 7. Snapshots of the LJ droplets (system 1). (a) One of the largest droplets (total 1805 molecules). (b) Smallest droplet obtained in system 1 (total 793 molecules). (c) Droplet grown in the ghost field at $\zeta = 1$ (state G in Figure 5a). (d) Reference droplet of the same density at $\zeta = 0$ (point R in Figure 5a).

to structure in distinct adsorbed layers that is typical for capillary condensate in a small spherical pore (Figure 8a). In the subsequent series of CEMC simulations, shown by horizontal dotted lines G → R in Figures 5a and 5b, the ghost field was gradually removed by incremental tuning of the host field magnitude ζ from 1 to 0. In the process of the ghost field removal, the density profile smoothens (Figures 8a−c), and the fluid partly evaporates, because the undisturbed ghost field reference droplet R at $\zeta = 0$ corresponds to a higher μ, $\mu_G < \mu_R$. The density profiles in Figure 8 are reckoned from the center of the cell. Due to droplet motion, they may differ from the density profiles calculated from the droplet center of mass.

4.2. Free Energy Calculation. *4.2.1. Thermodynamic Integration.* The continuity of the droplet isotherm in the full scale ghost field, $N_G(\mu)$, provided by the gauge cell method allows us to calculate the Helmholtz free energy $F_R(N,V,T)$ of the droplet state G (Figure 5) at overall loading $N_G = N_R$ in the ghost field by thermodynamic integration at constant temperature T and volume of the cell V

$$F_G(N_R) = -kN_G(\mu_{IG})T - \int_{\mu_{IG}}^{\mu_G} N_G(\mu)\, d\mu + \mu N_R \quad (13)$$

Here, we assume that the integration starts from an ideal gas state at $\mu = \mu_{IG}$.

To calculate the change of the Helmholtz free energy of the droplet state in the process of the ghost field being turned off, along the CEMC trajectory G → R ($\zeta = 1 \rightarrow \zeta = 0$), we employ the following scheme. Let us consider the Helmholtz free energy, $F_G(N_R,\zeta)$, of the fluid in the ghost field of the magnitude ζ. $F_G(N,1) = F_G(N_R)$ and $F(N_R,0) = F_D(N_R)$. $F(N,\zeta)$ is defined through the canonical partition function

$$Q(N,V,T,\zeta) = \frac{1}{\Lambda^{3N}N!}\int d\mathbf{r}^N \exp(-(\Phi(\mathbf{r}^N) + \zeta\Phi_G(\mathbf{r}^N))/kT) \quad (14)$$

as

$$F(N,V,T,\zeta) = -kT \ln Q(N,V,T,\zeta) \quad (15)$$

Here, $\Phi(\mathbf{r}^N)$ is the total potential energy of interactions between the molecules and between the molecules and the repulsive wall, and $\zeta\Phi_G(\mathbf{r}^N)$ is the potential energy of particle interaction with the ghost field of magnitude ζ. The derivative of F with respect to the host field magnitude is represented as the canonical ensemble average of the ghost field

$$\left.\frac{\partial F}{\partial \zeta}\right|_{N,V,T} = -kT\frac{1}{Q}\left.\frac{\partial Q}{\partial \zeta}\right|_{N,V,T} = \frac{\int d\mathbf{r}^N\, \Phi_G(\mathbf{r}^N)\exp(-(\Phi(\mathbf{r}^N) + \zeta\Phi_G(\mathbf{r}^N))/kT)}{\int d\mathbf{r}^N \exp(-(\Phi(\mathbf{r}^N) + \zeta\Phi_G(\mathbf{r}^N))/kT)} = \langle\Phi_G\rangle_{N,V,T,\zeta} \quad (16)$$

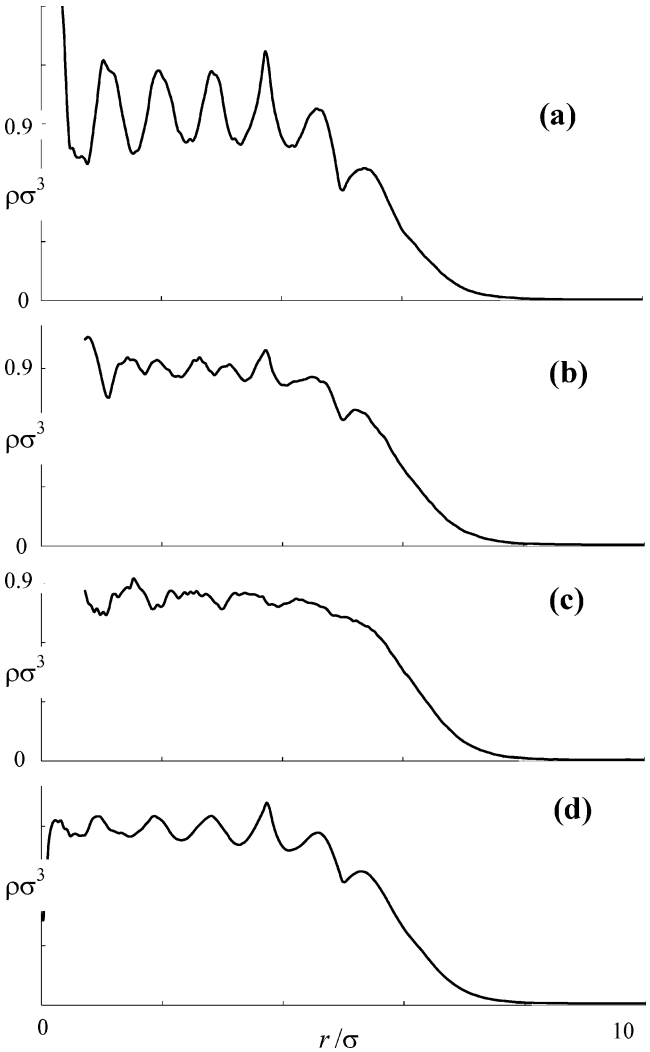

Figure 8. Local density profiles of droplets in system 1 simulated at a constant loading. (a) Droplet in the ghost field (state G, $\zeta = 1$). (b) Intermediate state, $\zeta = 0.4$. (c) $\zeta = 0$, reference droplet, state R. (d) Weighted local density profile $\rho_{GR}(r)$ applied for calculations of the free energy according to eq 21.

Here, $\langle\Phi_G\rangle_\zeta$ (subscripts N, V, and T are omitted for clarity) denotes the canonical ensemble average of the ghost field over the fluid configurations sampled in the ghost field of the magnitude ζ. $\langle\Phi_G\rangle_\zeta$ can be calculated by weighting the host field with the average fluid density $\rho_\zeta(\mathbf{r})$ in the ghost field of the magnitude ζ

$$\langle\Phi_G\rangle_{N,\zeta} = \int_V \Phi_G(\mathbf{r})\rho_\zeta(\mathbf{r})\,d\mathbf{r} \tag{17}$$

The evolution of the density profile $\rho(r)$ along the trajectory G → R is shown in Figure 8. Note that because the droplet motion is not constricted $\rho_\zeta(\mathbf{r})$ is not the average droplet density counted from the droplet center of mass.

Integration of the eq 16 along the CEMC trajectory gives a practical formula for calculating the Helmholtz free energy, F_G at loading N_R

$$F(N,\zeta) = F_G(N_R) - \int_\zeta^1 \langle\Phi_G\rangle_{N,\zeta}\,d\zeta = F_G(N_R) - \int_\zeta^1 \int_V \Phi_G(\mathbf{r})\rho_\zeta(\mathbf{r})\,d\mathbf{r}\,d\zeta \tag{18}$$

Thus, the sought Helmholtz free energy of the reference droplet state without the ghost field $F_D(N_R)$ is given by

$$F_D(N_R) = F_G(N_R) - W_{GR} \tag{19}$$

Here, W_{GR} is the reversible work of the host field removal that is equal to

$$W_{GR} = \int_0^1 \langle\Phi_G\rangle_\zeta\,d\zeta \tag{20}$$

Equation 20 implies a numerical integration whose accuracy depends on the number of CEMC simulations at different $\zeta = 1, ..., \zeta_I, \zeta_{I+1}, ..., 0$. An equivalent yet more practical formula is obtained by changing the order of integration in eq 17.

$$W_{GR} = \int_V \Phi_G(\mathbf{r})\rho_{GR}(\mathbf{r})\,d\mathbf{r} \tag{21}$$

Here, $\rho_{GR}(\mathbf{r})$ is the average local density in the droplet states along the CEMC trajectory computed by averaging over all sampled configurations. The profile of $\rho_{GR}(\mathbf{r})$ for system 1 is given in Figure 8d.

In practice, the ghost field method was implemented as follows. In system 1, the difference of free energies of the droplet configurations with and without the ghost field was estimated at $\rho_R = 0.0173\sigma^{-3}$ ($N_R = 1121$). In the course of the ghost field removal, the chemical potential is increased from $\mu_G = -9.03\epsilon$ ($\zeta = 1$ in -4ϵ ghost field) to $\mu_{\zeta=0.5} = -9.024\epsilon$ (G configuration in -2ϵ ghost field) to $\mu_R = -8.97\epsilon$ ($\zeta = 0$, reference state), which corresponded to an increase in supersaturation p_v/p_0 from 1.56 to 1.70. In system 2, we used the lowest number of molecules available for the calculation $N = 286$; $\mu_G = -8.019\epsilon$ (-2ϵ ghost field), $\mu_{\zeta=0.5} = -9.025\epsilon$ (G configuration in -1ϵ ghost field), and $\mu_R = -8.33\epsilon$. For the thermodynamic integration, we performed a series of 13 CEMC simulations for each system at $\zeta = 1, 0.9, 0.8, ..., 0.1, 0.05, 0.02, 0$.

As shown in Figure 9, despite the fact that the total loading is fixed, $\langle\Phi_G\rangle_\zeta$ increases monotonically from $\zeta = 1$ to $\zeta = 0$, because of a redistribution of molecules in the droplet as ζ decreases. At $\zeta = 1$, more molecules are located within the potential well, and the interface between the liquid droplet and vapor is sharper (Figure 7). The sharp increase of the magnitude of $\langle\Phi_G\rangle_\zeta$ at $\zeta \to 0$ (Figure 9) is caused by the droplet motion. $\langle\Phi_G\rangle_\zeta$ at $\zeta = 0$ is the potential energy of the fluid interaction with the full-scale ghost field averaged over the configurations of the reference droplet R and thus undisturbed by the ghost field. In this way, the droplet is not pinned and may move around the pore. Configurations A (droplet in the center) and

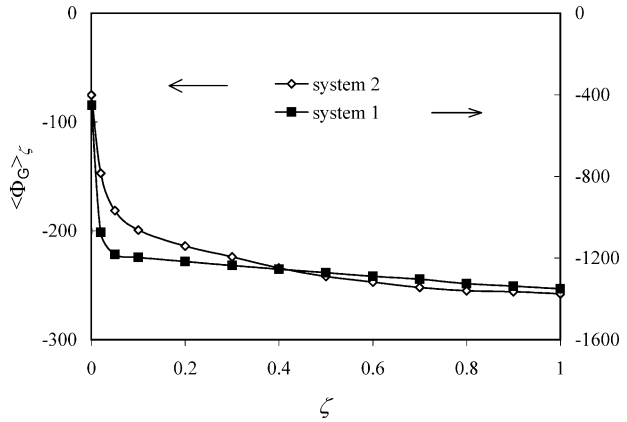

Figure 9. The contribution of the ghost field into the Helmholtz free energy $\langle\Phi_G\rangle_\zeta$ for systems 1 and 2, eq 17.

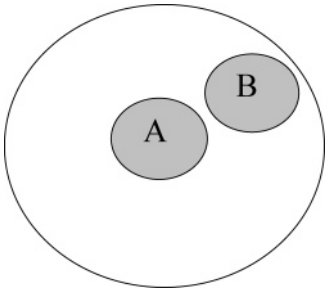

Figure 10. Schematic explanation of the sharp increase in $\langle\Phi_G\rangle_\zeta$ at $\zeta \to 0$. At $\zeta = 0$, configurations with the droplet in the center (A) and on the periphery (B) have a comparable statistical weight. However, only configuration A makes a substantial contribution to $\langle\Phi_G\rangle$. When ζ is appreciable ($\zeta > 0.05$), the droplet is always pinned to the potential well (configuration A).

B (droplet on the periphery) in Figure 10 have practically equal statistical weight. Yet, configuration A gives a large contribution to $\langle\Phi_G\rangle_\zeta$, while the contribution of configuration B is minute. The average density in the pore center is smaller than that of the fluid subjected to the ghost field. A possibility of droplet motion requires the use of smaller intervals $\Delta\zeta$ as $\zeta \to 0$. At larger ζ, the potential energy of fluid interaction with the ghost field keeps the droplet within the potential well located in the center of the cell. Although the location of the center of mass is allowed to fluctuate, the statistical weight of any configuration with the droplet located on the peripheral parts of the cell is close to zero.

Simulations with two different ghost fields, the depth of which differed by the factor of 2, provide a perfect test of the accuracy of the method. Apparently, the state in the deeper well at $\zeta = 0.5$ is equivalent to the state in the shallower well at $\zeta = 1$. Thus, the calculated Helmholtz free energy, $F(N_R,\zeta)$, in the deeper well at $\zeta \le 0.5$ should be equal to $F(N_R,2\zeta)$, as calculated in the shallower well. For system 2, we have obtained excellent agreement; the difference was just $2.4kT$. For system 1, we have obtained a substantial difference of ca. $18kT$. It is clear that that the method precision deteriorates when applied to larger systems because of a large compensation by the integral in the right part of eq 13

$$\int_{\mu_{IG}}^{\mu_R} N_G(\mu,T)\, d\mu$$

which is strongly negative, by $-W_{GR}$, which is strongly positive. For example, in system 1

$$\int_{\mu_{IG}}^{\mu_R} N_G(\mu,T)\, d\mu = -1797kT$$

for the deeper ghost field, and $-W_{GR} = 1658kT$. That is to say that a -4ϵ ghost field does not provide an acceptable estimate of the free energy barrier. The nucleation rate is proportional to the exponent of the nucleation barrier, which means that the absolute rather than the relative error should be taken into account. However, for system 2

$$\int_{\mu_{IG}}^{\mu_R} N_G(\mu,T)\, d\mu = -271kT$$

$-W_{GR} = 304kT$. Given the length and the accuracy of simulations for this system, the estimated statistical error of $2.5kT$ is very reasonable. The simulation scheme should be built in a way to avoid the compensation whenever possible. In particular, it is better to use a smaller droplet as a reference state and a weaker ghost field.

4.2.2. Umbrella Sampling. A powerful method to calculate the Helmholtz free energy is the umbrella sampling technique of Torrie and Valleau[37] (see ref 29), which we employed to check the accuracy of the thermodynamic integration. Equations 14 and 15 imply that the incremental difference in the Helmholtz free energy of two states sampled in CEMC simulation with the ghost field of magnitudes ζ_i and ζ_{i+1}, $\Delta F_{i+1,i}$, equals

$$\Delta F_{i+1,i} = -kT \ln \frac{\int dr^N \exp(-(\Phi(r^N) + \zeta_{i+1}\Phi_G(r^N))/kT)}{\int dr^N \exp(-(\Phi(r^N) + \zeta_i\Phi_G(r^N))/kT)} \quad (22)$$

$\Delta F_{i+1,i}$ can be expressed through the ensemble average at $\zeta = \zeta_i$ as

$$\Delta F_{i+1,i} = -kT \ln \langle \exp(-(\zeta_{i+1} - \zeta_i)\Phi_G/kT)\rangle_{\zeta_i} \quad (23)$$

As shown in ref 11, a better overlap of the sampled configurations, and respectively a better estimate, is achieved by using the ensemble average performed in the CEMC simulation with the ghost field of the intermediate magnitude $\zeta_i^* = \zeta_i + (\zeta_{i+1} - \zeta_I)/2$, defining

$$\Delta F_i = -kT \ln \frac{\langle \exp(-(\zeta_{i+1} - \zeta_i^*)\Phi_G/kT)\rangle_{\zeta_i^*}}{\langle \exp((\zeta_i^* - \zeta_i)\Phi_G/kT)\rangle_{\zeta_i^*}} \quad (24)$$

The total change of the Helmholtz free energy of the fluid gives the work of the ghost field removal

$$W_{GR} = \sum_i \Delta F_i \quad (25)$$

In the limit of $(\zeta_{i+1} - \zeta_i)\Phi_G(0)/kT \ll 1$, both methods, eqs 19 and 20 and eqs 24 and 25, are precise and give identical results.

To apply the umbrella sampling technique for estimation of ΔW_{GR}, CEMC states at ζ_i^* were generated using the regular canonical ensemble sampling with the canonical weighting function. At each state, the free energy difference ΔF_i between the states $\zeta_i^* - 0.05$ and $\zeta_i^* + 0.05$ was calculated according to eqs 22−24. For example, the result of the simulation at $\zeta^* = 0.45$ is the free energy difference between the configurations at $\zeta = 0.4$ and $\zeta = 0.5$. Figure 11 demonstrates the evaluation of $F(N,V,T) - F_G(N,V,T)$ with both methods, thermodynamic integration and umbrella sampling. Strictly speaking, the umbrella sampling technique is reliable when the droplet is centered in the center of the cell, because accounting for the cluster motion at lower ζ becomes problematic. In system 1, the total contribution of the ghost field to the potential energy totals about $-3000kT$ at $\zeta = 1$. Thus, the cluster is pinned to the potential well, although we do not impose any restriction to the location of the center of mass. Even at $\zeta = 0.01$, the ghost field produces a heavy bias to the location of the cluster in the cell. Thus, there may be no good overlap between the configurations at larger and smaller ζ. For example, configuration B in Figure 10 has a significant weight at $\zeta = 0$ but would have a negligible weight at $\zeta = 0.02$. Comparing the two techniques, we should note that the estimate of the statistical error for the umbrella sampling method is somewhat problematic, because it is hardly possible to evaluate whether the configurations obtained at a certain ζ are representative at $\zeta + \Delta\zeta$. As seen in Figure 11, which shows the augment of the Helmholtz free energy $F(N, V, T, \zeta + 0.5) - F(N, V, T, \zeta - 0.5)$, the two methods agree well with each other for system 1

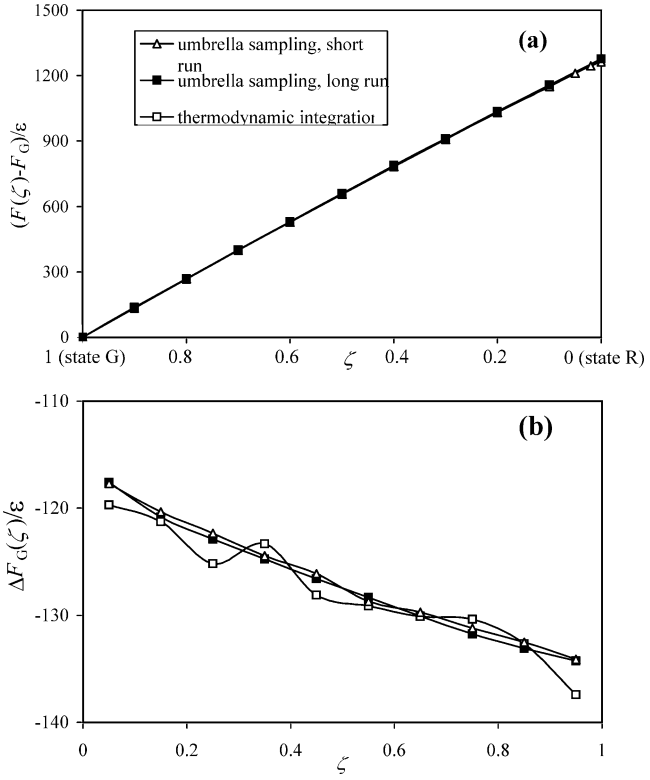

Figure 11. Variation of the Helmholtz free energy of the system associated with the ghost field removal. (a) Free energy related to that of state G, integral of Figure 9. (b) Free energy difference $\Delta F_G(\zeta)$ between the neighboring points (for example, point at $\zeta = 0.05$ is the difference between the free energies at $\zeta + 0.05$ and $\zeta - 0.05$). Solid squares, integration over ζ (eq 20) with equilibration over 50 000 steps per molecule in each single simulation; open squares, umbrella sampling over 150 000 steps per molecule (eqs 23 and 24); open triangles, same with umbrella sampling over 150 000 steps per molecule.

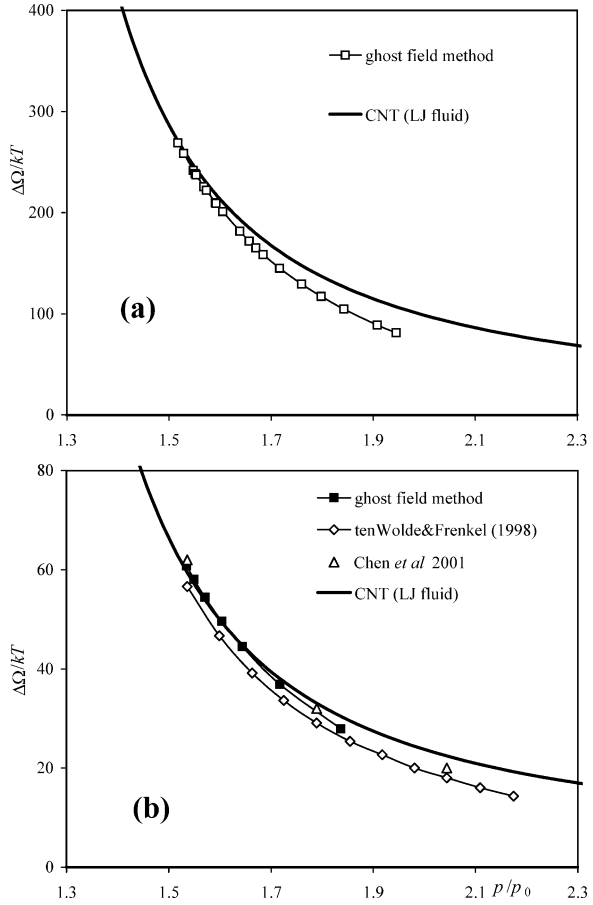

Figure 12. Nucleation barriers for droplet formation in an open system computed using the ghost field method (integration technique eqs 19−21). (a) System 1; (b) system 2. Solid lines, CNT predictions for a given LJ fluid, eq 11.

though the umbrella sampling gives somewhat larger fluctuations at the same simulation length. Numerically, the integration technique for obtaining W_{GR} is more consistent. The umbrella sampling technique gives larger fluctuations and is more expensive computationally.

5. Nucleation Barriers and Surface Tension

The nucleation barrier for the reference droplet at the chemical potential μ_{DR}, $\Delta\Omega(\mu_{DR},T)$, is calculated as

$$\Delta\Omega(\mu_R,T) = F_D(N_R,V,T) - \mu_R N_R - \Omega_v(\mu_R) \qquad (26)$$

where $\Omega_v(\mu_R)$ is the grand thermodynamic potential of the vapor state at $\mu = \mu_R$. Now, we can apply the nucleation theorem, eq 12, to calculate the variation of the nucleation barrier with the chemical potential or with the supersaturation, which is related to μ via the JZG equation of state.[47] The results are given in Figure 12. For system 1, we present the results obtained with the weaker ghost field of -2ϵ. We also plot the nucleation barriers predicted by the CNT model via eq 11 for a LJ fluid complied with the JZG equation of state. Despite a qualitative agreement, a quantitative comparison is problematic due to an uncertainty in the choice of the value of the surface tension discussed above. For system 1 ($r_c = 5\sigma$, $kT/\epsilon = 0.762$), we found values from 0.888 ϵ/σ^2 [49] to 0.922 ϵ/σ^2.[38] For system 2 ($r_c = 2.5\sigma$, $kT/\epsilon = 0.741$), interpolation of the recent simulation data[38,49,55] gives values of γ_∞ from 0.494 used in ref 5 for comparison to 0.580 ϵ/σ^2.[49] We used the same values employed for constructing the droplet isotherms in Figure 5; $\gamma_\infty = 0.91$ ϵ/σ^2 [48] for system 1, and $\gamma_\infty = 0.494$ ϵ/σ^2 [55] for system 2. Technically, it is possible to get a better agreement by fitting the surface tension in eq 10; however the agreement gained by fitting may be misleading.

For system 2, we also present the results of ten Wolde and Frenkel.[5] Given the difference in the definition of clusters discussed above, the agreement is quite reasonable; the difference varies from 1.5kT to 5kT. Our calculation gives a faster increase in the nucleation barriers with the droplet size that is consistent with the fact that our clusters have a larger excess mass ΔN^* at same μ (Figure 4d). Remarkably, three data points reported by Chen et al.[38] for this system practically coincide with ours. Chen et al.[38] employed a different cluster criterion than ten Wolde and Frenkel,[5] which hinders a reliable comparison of results.

It is tempting to discuss the dependence of the surface tension, which is related to the nucleation barrier, on the droplet size. Note that neither droplet radius nor the surface tension can be determined directly from MC data without invoking an equation of state to calculate equilibrium pressures and densities in respective bulk phases. To this end, we employ the JZG equation of state. The equimolar radius is determined from the excess droplet isotherm obtained in the MC simulation in accord with eq 1. Alternatively, one can determine the radius of tension of the spherical droplet in accord with the Laplace eq 2. The radius of tension must be used for a consistent estimate of the surface tension from the MC nucleation barrier based on the Gibbs eq 11. Thus, using different forms of eq 11, we can calculate the radius of tension r_s and the surface tension γ_s from $\Delta\Omega$ and

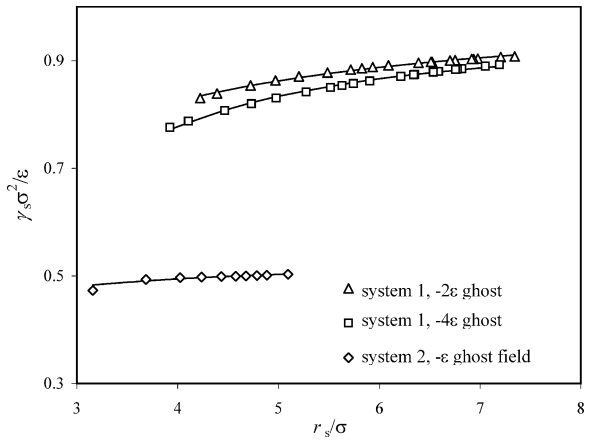

Figure 13. Dependence of the surface tension γ_s on the droplet size (radius of tension r_s). Data obtained with the weaker ghost field of -2ϵ is more reliable. We present the results obtained with the stronger ghost field -4ϵ to demonstrate the range of possible errors.

determine the dependence of the surface tension on the droplet radius $\gamma_s(r_s)$. This dependence is presented in Figure 13. In both systems, the surface tension increases monotonically with the droplet size and asymptotically approaches a constant value, which should be attributed to the planar surface tension γ_∞.

The results presented in Figure 13 can be interpreted by fitting the dependence $\gamma_s(r_s)$ with the Tolman equation[15]

$$\gamma = \gamma_\infty\left(1 - \frac{2\delta}{r_s}\right) \tag{27}$$

where γ_∞ is the limiting surface tension of a planar surface and δ is the Tolman length, which is assumed to be independent of the droplet size. Therewith, γ_∞ may be either taken from an independent simulation (as we did above in CNT calculations) or treated as a second adjustable parameter. Lines in Figure 13 show a fit to the simulation results obtained with the adjustable γ_∞. The simulation results are fitted nicely by the Tolman equation. We obtained $\gamma_\infty = 1.03\ \epsilon/\sigma^2$ and $\delta = 0.49$ and $1.01\ \epsilon/\sigma^2$ and $\delta = 0.38$ from the two simulation series discussed in the previous sections for system 1. However, the values of $\gamma_\infty > 1\ \epsilon/\sigma^2\gamma_\infty$ significantly exceed the highest value of $\gamma_\infty = 0.92\ \epsilon/\sigma^2$ [10] reported earlier in the literature for this LJ fluid, and the Tolman length values are too large. At the same time, the Tolman equation with parameters $\gamma_\infty = 0.91\ \epsilon/\sigma^2$ and $\delta = 0.2$ provides a reasonable fit in a narrower range of radii from 7.5σ to 6σ. This means that the results for system 1 cannot be fitted by the Tolman equation in the whole range of droplet radii. The best fit of the MC results for system 2 gives $\gamma_\infty = 0.54\ \epsilon/\sigma^2$ and $\delta = 0.15$, which can be considered as a reasonable estimate; although γ_∞ exceeds the value of $0.494\ \epsilon/\sigma^2$ [55] adopted above in the CNT model calculations, it is smaller than $0.580\ \epsilon/\sigma^2$ reported in ref 49. This analysis shows an ambiguity of interpretation of the size dependence of the surface tension in terms of the Tolman equation. This problem is discussed in detail elsewhere.[36]

7. Conclusion

A critical review of the molecular simulation approaches employed to study homogeneous nucleation of droplets in a metastable vapor shows that conventional methods have considerable drawbacks. A desirable approach should allow one to (a) stabilize a liquid cluster, which is entirely unstable in an open system, (b) determine the pressure or chemical potential in the surrounding vapor, (c) account for cluster motion within the simulation cell, (d) account for natural fluctuations of the cluster mass, (e) employ a rigorous thermodynamic definition of the cluster mass as an excess quantity rather then a geometrical prescription, and (f) calculate the cluster free energy and the nucleation barrier. A new MC simulation approach that we have developed fulfills these requirements. This approach exploits two simulation methods that we introduced and applied to modeling phase transitions in small pores, the gauge cell method[42,43] to generate the excess isotherm of droplet states and the ghost field method[11] to compute the nucleation barriers.

We considered the vapor-to-liquid transition in a LJ fluid confined to a spherical cell with repulsive walls, which is a case study for modeling homogeneous nucleation. To emphasize the key problems to be addressed in molecular simulations, we analyzed the specifics of the vapor-to-liquid transition in a finite volume using the capillarity approximation of the classical nucleation theory (the CNT model). Similarly to the recent work of Reguera et al.,[23] we demonstrated that the isotherm of droplet states in a closed system is not a monotonic function of the supersaturation; at a given loading (the total number of molecules), two types of droplet states are distinguished, a "large" D-droplet in a "low" density vapor and a "small" E-droplet in a denser vapor at a higher pressure. E-droplets are entirely unstable and correspond to the critical embryos for the vapor-to-droplet transition at a constant loading, resulting in the formation of a stable D-droplet. The minimum of the droplet isotherm corresponds to the superspinodal state of zero compressibility.[50a] The superspinodal marks the lower limit of sizes of D-droplets, which can be stabilized in canonical ensemble simulations. E-droplets cannot be generated in simulations. The superspinodal behavior makes construction of a continuous trajectory of droplet states for thermodynamic integration in a direct way impossible without invoking a stabilizing potential. This problem was solved by applying the ghost field MC simulation method.

We simulated two model LJ fluids: the LJ model nitrogen[53] at its normal boiling temperature of 77.4 K (5σ cutoff, $kT/\epsilon = 0.7625$) and the system studied earlier by ten Wolde and Frenkel[5] and Chen et al.[38] (2.5σ cutoff, $kT/\epsilon = 0.741$). The isotherms of vapor states were generated by the GCMC method, and the isotherms of D-droplets were generated by the gauge cell method. The gauge cell method was shown to be computationally efficient. It allows one to stabilize a droplet state by providing a controlled level of density fluctuations. The droplet mass is defined from the excess droplet isotherm without evoking any geometrical definition of a liquid cluster. There are no artificial constraints imposed on the droplet location. The chemical potential of the droplet state is measured directly. As expected from the CNT model analysis, the vapor-to-droplet and droplet-to-vapor transitions occurred spontaneously at different loadings, forming a horizontal hysteresis loop. As the superspinodal is approached, D-droplet states become kinetically unstable, and thus, it is not possible to continue the droplet isotherm to smaller droplets. The superspinodal marks the smallest droplet that can be stabilized by reducing the gauge cell capacity to zero, which corresponds to the closed system in the canonical ensemble. We found that the droplet isotherms are in a qualitative agreement with predictions of the CNT model for a given LJ fluid. However, a quantitative comparison is hindered due to an uncertainty in the value of the surface tension. At the same time, we found a reasonable agreement with earlier simulations of ten Wolde and Frenkel[5] and Chen et al.,[38] who employed different umbrella sample techniques. The gauge cell method makes constructing the excess isotherm of droplet states

in a wide range of droplet sizes (up to 2000 molecules in system 1) possible, which is limited from below by the superspinodal. To extend the isotherm to smaller droplets, the size of the simulation cell must be reduced. A prominent example of the efficient use of cells of different size is presented elsewhere.[56] Since the droplet stabilized in the closed system by using the gauge cell method corresponds to the critical nucleus in an open system at the same chemical potential, the constructed excess isotherm represents the isotherm of critical nuclei.

The excess isotherm of droplets can be employed to calculate the nucleation barrier of vapor−liquid transition in accord with the nucleation theorem, eq 7, provided the nucleation barrier for a reference cluster is determined independently. We applied the ghost field method[11] to construct a continuous trajectory of states connecting a reference cluster and a low-density vapor state and to determine the cluster free energy by the thermodynamic integration along this trajectory. Special attention was paid to the implementation and technical details of the ghost field method.

Within the ghost field method, a reference cluster is constructed in two series of simulations. First, a droplet of a given density stabilized by a ghost filed potential is generated in a continuous manner starting from a low-density vapor in a series of gauge cell simulations. The ghost field potential represents a potential well located in the cell center. As the vapor pressure increases, vapor condenses in the well, forming a growing cluster pinned to the well. We employed two ghost fields with different depths of the potential wells to check the method consistency and accuracy. Second, the ghost field is gradually removed in a series of CEMC simulations, keeping the fluid density fixed and decreasing the ghost field magnitude ζ from 1 to 0. In the terminology of adsorption science, the trajectory of equilibrium states obtained at fixed temperature, volume, and density/loading by varying the magnitude of the external field can be referred to as an "isothermal isostere". The reference cluster, undisturbed by the ghost field, is stabilized by the gauge cell method to determine its chemical potential. We analyzed the effect of cluster depinning; as the ghost field is turned off the cluster becomes free to move around the cell.

The work of formation of the reference cluster is calculated as the difference between the work of cluster formation in the ghost field applied and the work of the ghost field removal. The former is calculated by direct integration of the isotherm of cluster condensation in the ghost field. This isotherm is continuous and has a sigmoidal van der Waals shape typical for capillary condensation in small pores. To compute the work of the ghost field removal, we introduced and examined two different schemes. The first, which is recommended as the most efficient, is based on direct thermodynamic integration of the contributions of the ghost field into the Helnholtz free energy along the isothermal isostere. The other exploits the umbrella sampling method for calculating the free energy difference of the states along the isostere. We showed that these methods produce identical results; however due to the depinning effect, the umbrella sampling requires more frequent simulation points to provide comparable accuracy. We concluded that the best accuracy of the free energy calculations is achieved by employing the smallest reference droplet stabilizable in the gauge cell method and the weakest ghost field sufficient to grow this droplet in a continuous manner.

We determined the nucleation barriers for droplets containing from 260 to 2000 molecules of up to 7.5 molecular diameters. The simulation results were found to be in qualitative agreement with the CNT model of a JZG LJ fluid. However, quantitative assessment is hindered due to an uncertainty in the planar surface tension. We have also found that the size dependence of the surface tension cannot be described by the Tolman equation with sufficient accuracy. The difference between the radius of tension and the equimolar radius defined from the MC simulations depends on the cluster size. The data that we reported can serve as a touchstone to verify theoretical conclusions.

Good agreement was found for the system studied earlier by ten Wolde and Frenkel[5] and Chen et al.[38] (2.5σ cutoff, $kT/\epsilon = 0.741$). However, it is difficult to make solid conclusions since different cluster criteria were used in these works. It is worth noting that our method does not involve any cluster criterion and is based on the rigorous thermodynamic definition of the cluster mass through the excess quantity. This makes the method robust and versatile. It is applicable to other nucleation processes more complex than the droplet nucleation in LJ fluid considered here. The problem of bridging in nanochannels considered in ref 11 gives an instructive example of the method's applicability to a system, which could hardly be studied by other methods.

Acknowledgment. The work is supported by the TRI/Princeton exploratory research program. A.V.N. thanks the John Simon Guggenheim Memorial Foundation for a 2004 Guggenheim Fellowship.

Supporting Information Available: Figures showing the literature data on the surface tension of a bulk Lennard-Jones fluid, the dependence of the minimum radius of the cluster on the radius of the cell, and the isotherms of LJ fluid in a smaller pore. This material is available free of charge via the Internet at http://pubs.acs.org.

References and Notes

(1) McGinty, D. J. *J. Chem. Phys.* **1971**, *55*, 580.
(2) Lee, J. K.; Barker, J. A.; Abraham, F. F. *J. Chem. Phys.* **1973**, *58*, 3166−3180.
(3) Rusanov, A. I.; Brodskaya, E. N. *J. Colloid Interface Sci.* **1977**, *62*, 542−555.
(4) Nijmeijer, M. J. P.; Bruin, C.; van Woerkom, A. B.; Bakker, A. F.; van Leeuwen, J. M. J. *J. Chem. Phys.* **1992**, *96*, 565−576.
(5) ten Wolde, P. R.; Frenkel, D. *J. Chem. Phys.* **1998**, *109*, 9901−9918.
(6) Kusaka, I.; Oxtoby, D. W. *J. Chem. Phys.* **1999**, *110*, 5249−5261.
(7) Kusaka, I.; Wang, Z. G.; Seinfeld, J. H. *J. Chem. Phys.* **1998**, *108*, 3416−3423.
(8) Moody, M. P.; Attard, P. *Phys. Rev. Lett.* **2003**, *91*.
(9) MacDowell, L. G.; Virnau, P.; Miller, M.; Binder, K. *J. Chem. Phys.* **2004**, *120*, 5293−5302.
(10) Chen, B.; Siepmann, J. I. *J. Phys. Chem. B* **2000**, *104*, 8725−8734.
(11) Vishnyakov, A.; Neimark, A. V. *J. Chem. Phys.* **2003**, *119*, 9755−9754.
(12) McGinty, D. J. *J. Chem. Phys.* **1973**, *58*, 4733−4742.
(13) Kristensen, D. W.; Jensen, E. J.; Cotteril, R. M. *J. Chem. Phys.* **1974**, *60*, 4161−4169.
(14) Briant, C. L.; Burton, J. J. *J. Chem. Phys.* **1975**, *63*, 2045−2058.
(15) Tolman, R. C. *J. Chem. Phys.* **1949**, *17*, 333−337.
(16) Lee, J. K.; Barker, J. A.; Pound, G. M. *J. Chem. Phys.* **1974**, *60*, 1976−1980.
(17) Barker, J. A.; Henderson D. *J. Chem. Phys.* **1967**, *47*, 4714.
(18) Toxvaerd, S. *J. Chem. Phys.* **1971**, *55*, 3116.
(19) Barker, J. A.; Henderson D. *Annu. Rev. Phys. Chem.* **1972**, *23*, 439.
(20) Garcia, N. G.; S, T. J. M. *Phys. Rev. Lett.* **1981**, *47*, 186−190.
(21) Weakliem, C. L.; Reiss, H. *J. Chem. Phys.* **1993**, *99*, 5374−5383.
(22) Oh, K. J.; Zeng, X. C. *J. Chem. Phys.* **1998**, *108*, 4683−4684.
(23) Reguera, D.; Bowles, R. K.; Djikaev, Y.; Reiss, H. *J. Chem. Phys.* **2003**, *118*, 340−353.
(24) Reiss, H.; Katz, J. L.; Cohen, E. R. *J. Chem. Phys.* **1968**, *48*, 5553.
(25) Binder, K.; Kalos, M. H. *J. Stat. Phys.* **1980**, *22*, 363.
(26) (a) Binder, K. *Physica A* **2003**, *319*, 99−114. (b) Kiessling, M. K.-H.; Percus, J. K. *J. Stat. Phys.* **1995**, *78*, 1337.
(27) Reiss, H.; Reguera, D. *J. Phys. Chem. B* **2004**, *108*, 6555−6563.
(28) Widom, B. *J. Chem. Phys.* **1963**, *39*, 2808.

(29) Frenkel, D.; Smit, B. *Understanding Molecular Simulation. From Algorithms to Applications*; Academic Press: San Diego, 1996.
(30) Irving, J. H.; Kirkwood, J. G. *J. Chem. Phys.* **1950**, *18*, 817−829.
(31) Thompson, S. M.; Gubbins, K. E.; Walton, J.; Chantry, R. A. R.; Rowlinson, J. S. *J. Chem. Phys.* **1984**, *81*, 530−542.
(32) Brodskaya, E. N.; Rusanov, A. I. *J. Chem. Phys.* **1994**, *100*, 7844−7844.
(33) Nijmeijer, M. J. P.; Bruin, C.; van Leeuwen, J. M. J. *J. Chem. Phys.* **1994**, *100*, 7844−7844.
(34) Haye, M. J.; Bruin, C. *J. Chem. Phys.* **1994**, *100*, 556.
(35) El Bardouni, H.; Mareschal, M.; Lovett, R.; Baus, M. *J. Chem. Phys.* **2000**, *113*, 9804−9809.
(36) Neimark, A. V.; Vishnyakov, A. *J. Chem. Phys.* **2005**, 122, 054707.
(37) Torrie, G. M.; Valleau, J. P. *J. Comput. Phys.* **1977**, *23*, 187−199.
(38) Chen, B.; Siepmann, J. I.; Oh, K. J.; Klein, M. L. *J. Chem. Phys.* **2001**, *115*, 10903−10913.
(39) Chen, B.; Siepmann, J. I. *J. Phys. Chem. B* **2001**, *105*, 11275−11282.
(40) Norman, G. E.; Filinov, V. S. *High Temp.* **1969**, *7*, 216-&.
(41) Hale, B. N. *Aust. J. Phys.* **1996**, *49*, 425−434.
(42) Neimark, A. V.; Vishnyakov, A. *Phys. Rev. E* **2000**, *62*, 4611−4622.
(43) Vishnyakov, A.; Neimark, A. V. *J. Phys. Chem. B* **2001**, *105*, 7009−7020.
(44) Gibbs, J. W. *The Scientific Papers of J. Willard Gibbs*; Dover: New York, 1961; Vol. 1.
(45) Ono, S.; Kondo, S. In *Encyclopedia of Physics*; Flugge, S., Ed.; Springer: Berlin, 1960; Vol. 10.
(46) Rowlinson, J. S.; Widom, B. *Molecular Theory of Capillarity*; Clarendon: Oxford, 1982.
(47) Johnson, J. K.; Zollweg, J. A.; Gubbins, K. E. *Mol. Phys.* **1993**, *78*, 591−618.
(48) Errington, J. R. *Phys. Rev. E* **2003**, *67*.
(49) Mecke, M.; Winkelmann, J.; Fischer, J. *J. Chem. Phys.* **1997**, *107*, 9264−9270.
(50) (a) Neimark, A. V.; Ravikovitch, P. I.; Vishnyakov, A. *Phys. Rev. E* **2002**, *65*, 031505. (b) Lee, D. J.; TeloDaGamma, M. M.; Gubbins, K. E. *J. Chem. Phys.* **1986**, *85*, 490−499.
(51) Kashchiev, D. *J. Chem. Phys.* **2003**, *118*, 9081−9083.
(52) Viisanen, Y.; Strey, R.; Reiss, H. *J. Chem. Phys.* **1993**, *99*, 4680−4692.
(53) Ravikovitch, P. I.; Vishnyakov, A.; Russo, R.; Neimark, A. V. *Langmuir* **2000**, *16*, 2311−2320.
(54) Peterson, B. K.; Gubbins, K. E. *Mol. Phys.* **1987**, *62*, 215−226.
(55) Holcomb, C. D.; Clancy, P.; Zollweg, J. A. *Mol. Phys.* **1993**, *78*, 437−459.
(56) Neimark, A. V.; Vishnyakov, A. *J. Chem . Phys.*, in press.